



The Common Envelope Origins of the Fast Jet in the Planetary Nebula M 3–38

J. S. Rechy-García¹ , J. A. Toalá^{1,5} , M. A. Guerrero² , C. Rodríguez-López² , L. Sabin³ , and G. Ramos-Larios⁴ ¹Instituto de Radioastronomía y Astrofísica, UNAM, Antigua Carretera a Pátzcuaro 8701, Ex-Hda. San José de la Huerta, Morelia 58089, Mich., Mexico; j.rechy@irya.unam.mx²Instituto de Astrofísica de Andalucía, IAA-CSIC, Glorieta de la Astronomía S/N, E-18008 Granada, Spain³Instituto de Astronomía, UNAM, Apdo. Postal 877, Ensenada 22860, B.C., Mexico⁴Instituto de Astronomía y Meteorología, CUCEI, Universidad de Guadalajara, Av. Vallarta 2602, Arcos Vallarta, 44130 Guadalajara, Mexico

Received 2022 March 18; revised 2022 June 13; accepted 2022 June 15; published 2022 July 6

Abstract

We present the analysis of Multi-Espectrógrafo en GTC de Alta Resolución para Astronomía (MEGARA) high-dispersion integral field spectroscopic observations of the bipolar planetary nebula (PN) M 3–38. These observations unveil the presence of a fast outflow aligned with the symmetry axis of M 3–38 that expands with a velocity of up to $\pm 225 \text{ km s}^{-1}$. The deprojected space velocity of this feature can be estimated to be $\approx 320_{-60}^{+130} \text{ km s}^{-1}$, which together with its highly collimated morphology suggests that it is one of the fastest jets detected in a PN. We have also used Kepler observations of the central star of M 3–38 to unveil variability associated with a dominant period of 17.7 days. We attribute this to the presence of a low-mass star with an orbital separation of $\approx 0.12\text{--}0.16 \text{ au}$. The fast and collimated ejection and the close binary system point toward a common envelope formation scenario for M 3–38.

Unified Astronomy Thesaurus concepts: Planetary nebulae (1249); Stellar jets (1607); Stellar winds (1636); Low mass stars (2050)

1. Introduction

Planetary nebulae (PNe) are formed by mass lost by solar-like stars on their way to becoming white dwarfs, mostly during the asymptotic giant branch (AGB) phase (Vassiliadis & Wood 1993). The resultant stellar remnant becomes hot enough to produce a high UV flux and a fast stellar wind that ionizes and compresses the material ejected in the late AGB phase, giving birth to a PN (Kwok 2000).

It has long been suggested that the generalized interacting stellar winds model of PN formation (Balick 1987) is too simple to explain the wide variety of PN morphologies (e.g., Schwarz et al. 1992; Manchado et al. 1996). Several mechanisms were soon invoked to explain this conundrum (Soker 1997), involving binary star interactions, and including jet-like ejecta during the late AGB or early post-AGB phases (Sahai & Trauger 1998).

Jets or bipolar fast outflows have been known to exist in PNe for a long time since their first discovery in NGC 2392 (Giesekeing et al. 1985). The statistical analysis of a sample of 85 collimated outflows detected in 58 PNe (Guerrero et al. 2020 and references therein) found a bimodal distribution, with $\approx 30\%$ of collimated outflows showing velocities $\geq 100 \text{ km s}^{-1}$. These high-velocity jets are prime candidates to have been launched by a binary system at the core of the PN.

The presence of fast collimated outflows can be gleaned by observing images of PNe as their action is typically associated with highly elongated structures, S-shaped filaments, and V-shaped structures (Rechy-García et al. 2020a).

⁵ Visiting astronomer at the Instituto de Astrofísica de Andalucía (IAA-CSIC, Spain) as part of the Centro de Excelencia Severo Ochoa Visiting-Incoming program

Complementary kinematical information has been traditionally obtained using long-slit high-dispersion spectroscopic observations, which are otherwise the only method to detect fast collimated outflows in compact PNe (Rechy-García et al. 2017). The advent of high-dispersion integral field spectroscopy provides kinematical information with broad spatial coverage. This technique has allowed, for instance, the extension of the extremely faint bipolar jet in NGC 2392 to be mapped for the first time (Guerrero et al. 2021), the dissection of the abundances and kinematics of the born-again PN HuBi 1 (Rechy-García et al. 2020b; Montoro-Molina et al. 2022), and the study of the spatiokinematical structure of M 2–31 (Rechy-García et al. 2021).

In this Letter, we present the discovery of one of the fastest collimated outflows in a PN. We use Multi-Espectrógrafo en GTC de Alta Resolución para Astronomía (MEGARA; Gil de Paz et al. 2018) observations obtained at the Gran Telescopio Canarias (GTC) of the PN M 3–38 (PN G356.9+04.4) to unveil its extreme kinematic structure. Its central star (CSPN) is further found to exhibit a Kepler/K2 light curve consistent with a post-common envelope (post-CE) binary system, which can be blamed as responsible for the collimation of the fast outflow in the recent past. The observations and archival data analysis of M 3–38 were motivated by the presence of extremely fast ejecta revealed in the long-slit echelle spectrum of the $H\alpha$ + [N II] emission lines available at the San Pedro Mártir Spectroscopic Catalogue of PNe (López et al. 2012) and by the highly elongated bipolar morphology displayed in a narrow-band Hubble Space Telescope (HST) WFPC2 F656N image (see Figure 14 in Guzman-Ramirez et al. 2014).

This Letter is organized as follows. In Section 2 we describe the observations and the data preparation, in Section 3 we present our results, and finally, a discussion is given in Section 4.

2. Observations and Data Preparation

M 3–38 was observed with GTC MEGARA on 2021 August 29 using the Integral Field Unit (IFU) mode. This provides a field of view of $12''.5 \times 11''.3$ with a spaxel size of $0''.62$. We used the high-resolution (HR) volume-phased holographic (VPH) grism VPH665-HR covering the 6405.6–6797.1 Å wavelength range at a spectral dispersion of 0.098 \AA with a resolution of $R = 18,700$ ($\simeq 16 \text{ km s}^{-1}$). Three 900 s exposures were obtained with a seeing of $1''.2$.

The data reduction process was carried out using the Data Reduction Cookbook provided by the Universidad Complutense de Madrid (Pascual et al. 2019). Through the pipeline, we subtracted the sky and bias contributions, corrected for flat-field effects, and performed wavelength calibration, spectra tracing, and extraction. Sky subtraction is performed via 56 ancillary fibers located $\approx 2''.0$ from the center of the IFU. We apply the regularization grid task `megarars2cube`⁶ to obtain square spaxels with sizes of $0''.215$. The final cube has dimensions of $52 \times 58 \times 4300$ equivalent to a total of 3016 spectra in the datacube. The flux calibration was done using observations of the spectrophotometric standard star HR 7596 taken immediately after the observations of M 3–38.

M 3–38 was observed by the Kepler/K2 mission (Howell et al. 2014) during Campaign 11 in 2016 from September 24 to December 8. Campaign 11 suffered a three-day interruption (October 18–20) to make a pointing correction of $-0''.32$ in the spacecraft attitude. As a result, the data set was split into two parts, designated Campaigns 111 and 112, spanning 23 and 48 days, respectively (see Figure 5, upper left), that were processed separately using new target apertures in the second part of the campaign (see the Data Release Notes⁷ for more information). We retrieved the two light curves from the Mikulski Archives for Space Telescopes⁸ and used the Pre-search Data Conditioning Simple Aperture Photometry (PDCSAP) data sets, already cleaned for systematic errors. After removing outliers, the flux was normalized and the two data sets were joined together, resulting in a total of 3166 useful points with a 30 minute cadence along a 74 day time baseline.

3. Results

3.1. Kinematics of the Collimated Outflow

The MEGARA IFS observations of M 3–38 indicate diffuse emission in the $\text{H}\alpha$, $[\text{N II}] \lambda\lambda 6548, 6584$, $[\text{S II}] \lambda\lambda 6717, 6731$, and $\text{He II } \lambda 6560$ lines. Emission from the $[\text{N II}] \lambda\lambda 6435.61, 6527.23$, $\text{C I } \lambda\lambda 6674.11, 6683.95$, and $\text{C II } \lambda 6578.05$ lines is also detected in the innermost regions. The spatio-kinematics of M 3–38 will be investigated here using the brightest $\text{H}\alpha$ and $[\text{N II}] \lambda 6584$ emission lines.

A tomographic view of M 3–38 is displayed in Figure 1, with channel maps of the $[\text{N II}] \lambda 6584$ emission line spanning from radial velocities in the range of -480 to $+160 \text{ km s}^{-1}$ with a width of 40 km s^{-1} . For a systemic velocity in the Local Standard of Rest (LSR) frame of $v_{\text{sys}} = -160.5 \text{ km s}^{-1}$ (central panel of Figure 1), the emission in the most extreme panels

implies expansion velocities in the range of $\pm 225 \text{ km s}^{-1}$. The emission of the fast outflow of M 3–38 is aligned along a position angle (PA) of $43^\circ \pm 2^\circ$, with the southwest emission approaching (blueshifted) and the northeast emission receding (redshifted). The emission is thus mostly aligned with the symmetry axis of M 3–38, as illustrated in the left panel of Figure 2, where contours of the emission in different velocity ranges are overplotted on an HST WFPC2 $\text{H}\alpha$ image. In this image, M 3–38 exhibits a highly axisymmetric morphology with two bipolar lobes $5''.3$ in size aligned along a PA of $39^\circ \pm 6^\circ$ terminating in bow-shock-like clumps. The emission from the intermediate-velocity ranges from -40 to 0 km s^{-1} (orange in Figure 2, left) and -320 to -280 km s^{-1} (blue in Figure 2, left) is associated with those clumps, but the emission from the extreme-velocity ranges from $+80$ to $+120 \text{ km s}^{-1}$ (red in Figure 2, left) and -400 to -360 km s^{-1} (violet in Figure 2, left) peaks at $\simeq 5''$ from the CSPN, i.e., they extend beyond the emission detected in the HST $\text{H}\alpha$ image.

The extent of the emission detected by MEGARA is illustrated in the continuum-subtracted $\text{H}\alpha$ and $[\text{N II}] \lambda 6584$ maps presented in Figure 3. A density map is also presented in the right panel of this figure. The density has been computed from the $[\text{S II}] \lambda 6716$ to $[\text{S II}] \lambda 6731$ ratio map using the `PyNeb` package (Luridiana et al. 2015) for the analysis of emission lines assuming an electron temperature⁹ of $10,000 \text{ K}$. This map indicates a clear density gradient from the innermost regions of M 3–38 to the inner outflow ($N_e \approx 2500 \text{ cm}^{-3}$) to its outermost tip ($N_e \approx 1500 \text{ cm}^{-3}$).

To investigate the expansion law of the outflow of M 3–38, classical position–velocity (PV) diagrams in the $\text{H}\alpha$ and $[\text{N II}] \lambda 6584$ emission lines have been extracted from a pseudo-long slit along its bipolar axis at PA 45° (Figure 4, top). These PV diagrams are consistent with a homologous expansion with a velocity gradient of $\approx 60 \text{ km s}^{-1} \text{ arcsec}^{-1}$. We note that these PV diagrams are suggestive of a double-S shape that could be attributed to precession. The highest-velocity components at the tip of this outflow reach expansion velocities of $\pm 220 \text{ km s}^{-1}$, with the SW clump showing an intriguing hook-like shape extending up to $\approx 7''$ from the CSPN with an expansion velocity of -240 km s^{-1} .

The MEGARA observations also detect another pair of high-velocity clumps, as denoted by the violet and red contours in Figure 2, left, located $\simeq 5''.5$ from the CSPN toward the SE and NW of M 3–38, respectively. Quite surprisingly, these clumps are aligned along a direction that is almost orthogonal to the bipolar axis of M 3–38. To illustrate further their presence, $\text{H}\alpha$ and $[\text{N II}] \lambda 6584$ PV diagrams have also been extracted from a $1''$ -wide pseudo-long slit along PA $= 320^\circ$ (Figure 2, right). These PV diagrams (Figure 4, bottom), and particularly the $[\text{N II}]$ one, confirm the presence of high-velocity components with an expansion velocity of $\pm 230 \text{ km s}^{-1}$ along this direction.

Incidentally, we shall mention that the PV diagrams shown in Figure 4 reveal the presence of an extended component at the systemic velocity of M 3–38 that seems to fill the whole field of view of the MEGARA IFU. This component is broad and unresolved, with an intrinsic FWHM of 40 km s^{-1} and a line

⁶ Task developed by J. Zaragoza-Cardiel available at <https://github.com/javierzaragoza/megarars2cube>.

⁷ https://archive.stsci.edu/missions/k2/doc/dm/KSCI-19151-002_K2-DRN30_C11.pdf

⁸ <https://mast.stsci.edu/portal/Mashup/Clients/Mast/Portal.html>

⁹ The calculation of the density using the $[\text{S II}]$ doublet is rather insensitive to the adopted value of electron temperature for typical values in the range 8000 – 12000 K found in PNe.

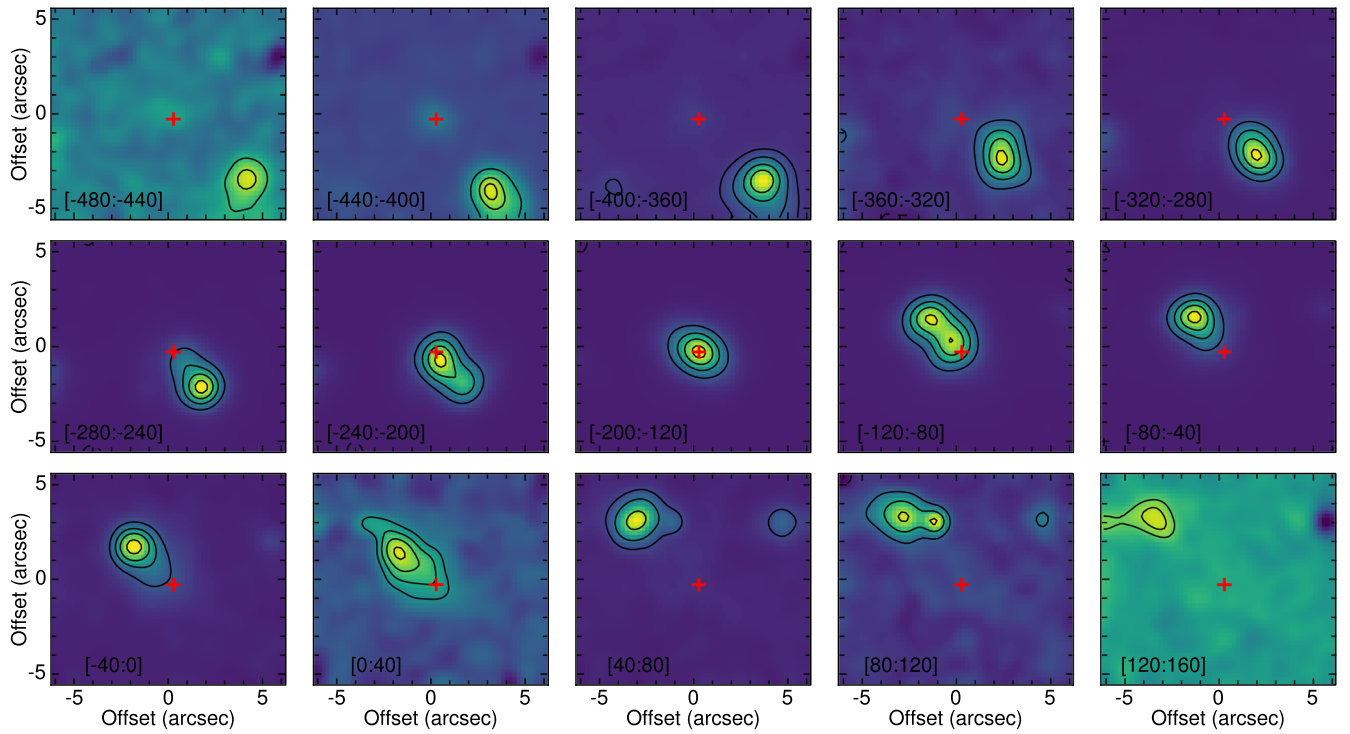


Figure 1. GTC MEGARA tomography of M 3–38 in the [N II] $\lambda 6584$ emission line. The LSR velocity range is labeled at the bottom-left corner of each panel. The central frame corresponds to the systemic velocity. The red “cross” indicates the location of the CSPN of M3–38, as determined from the emission of the stellar continuum, which is consistent with the central position of the nebular waist. North is up, east is to the left.

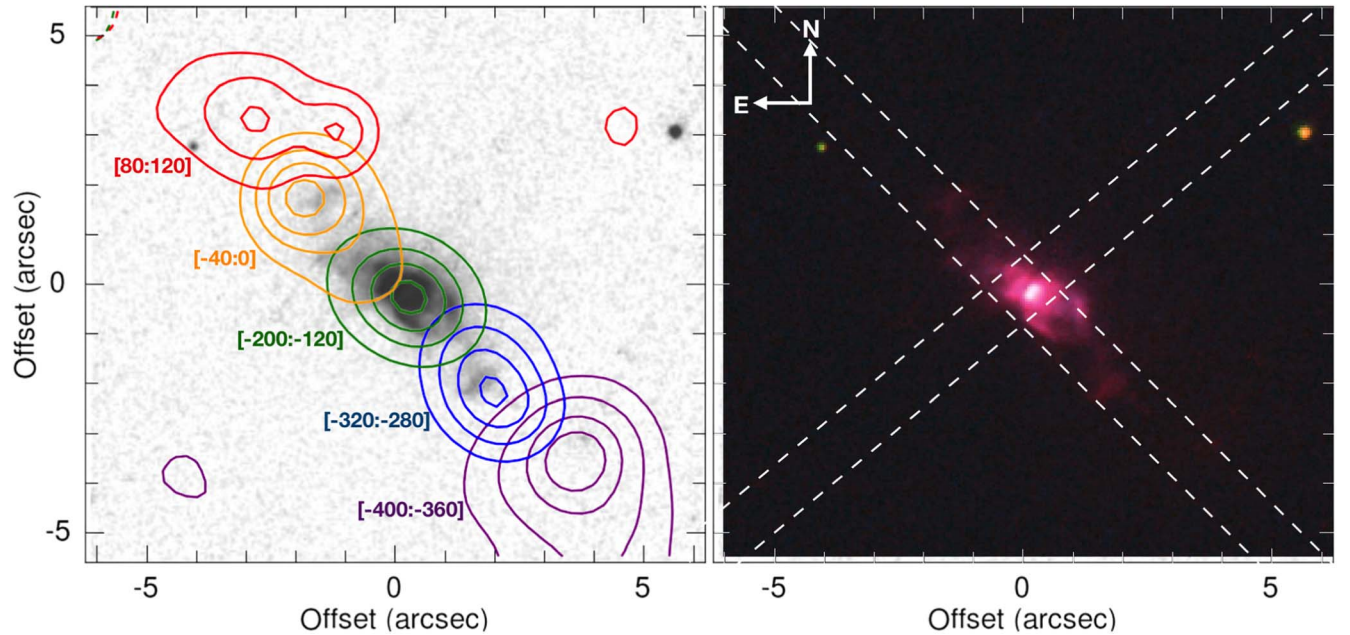


Figure 2. HST WFPC2 optical images of M 3–38. The left panel shows a gray-scale F656N ($H\alpha$) image imposed with contours from the MEGARA [N II] $\lambda 6584$ Å emission line. The colors represent different velocity ranges as labeled. The right panel shows a color-composite image obtained by combining F656N $H\alpha$ (red), F547M (green), and F502N [O III] (blue) images. The dashed-line areas represent the extraction regions for the PV diagrams shown in Figure 4.

tilt of up to $\simeq 6 \text{ km s}^{-1}$. It can thus be interpreted as a low-velocity nonspherical halo around M 3–38.

3.2. Photometric Variations of the Central Star

We used Period04 (Lenz & Breger 2005) to search for periodicities in the Kepler/K2 light curve of the CSPN of M 3–38 derived from Campaigns C111 and C112 (Figure 5, top

left). The amplitude spectra were calculated up to the Nyquist frequency, corresponding to $24 \text{ cycles days}^{-1}$. A frequency is considered significant when its amplitude is at least four times the noise level (Breger et al. 1993), which is equivalent to a 99.9% confidence level (Kuschnig et al. 1997). Because no significant frequencies were found in the high-frequency range, the original light curve was binned into one-day bins to search for periodicities up to the $0.5 \text{ cycle day}^{-1}$ Nyquist limit

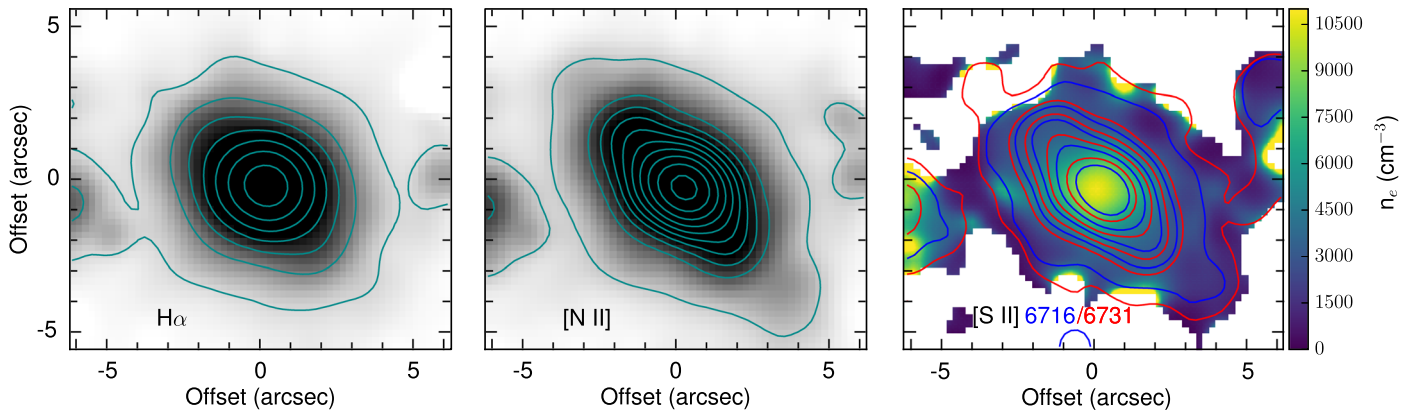


Figure 3. GTC MEGARA continuum-subtracted H α (left) and [N II] λ 6584 (center) line emission maps, and electron density map derived from the [S II] $\lambda\lambda$ 6716,6731 line ratio (right; see text for details). Contours are used to emphasize regions both faint and bright surface brightness. The blue and red contours in the density map correspond to the same surface brightness levels in the [S II] λ 6716 and [S II] λ 6731 images, respectively.

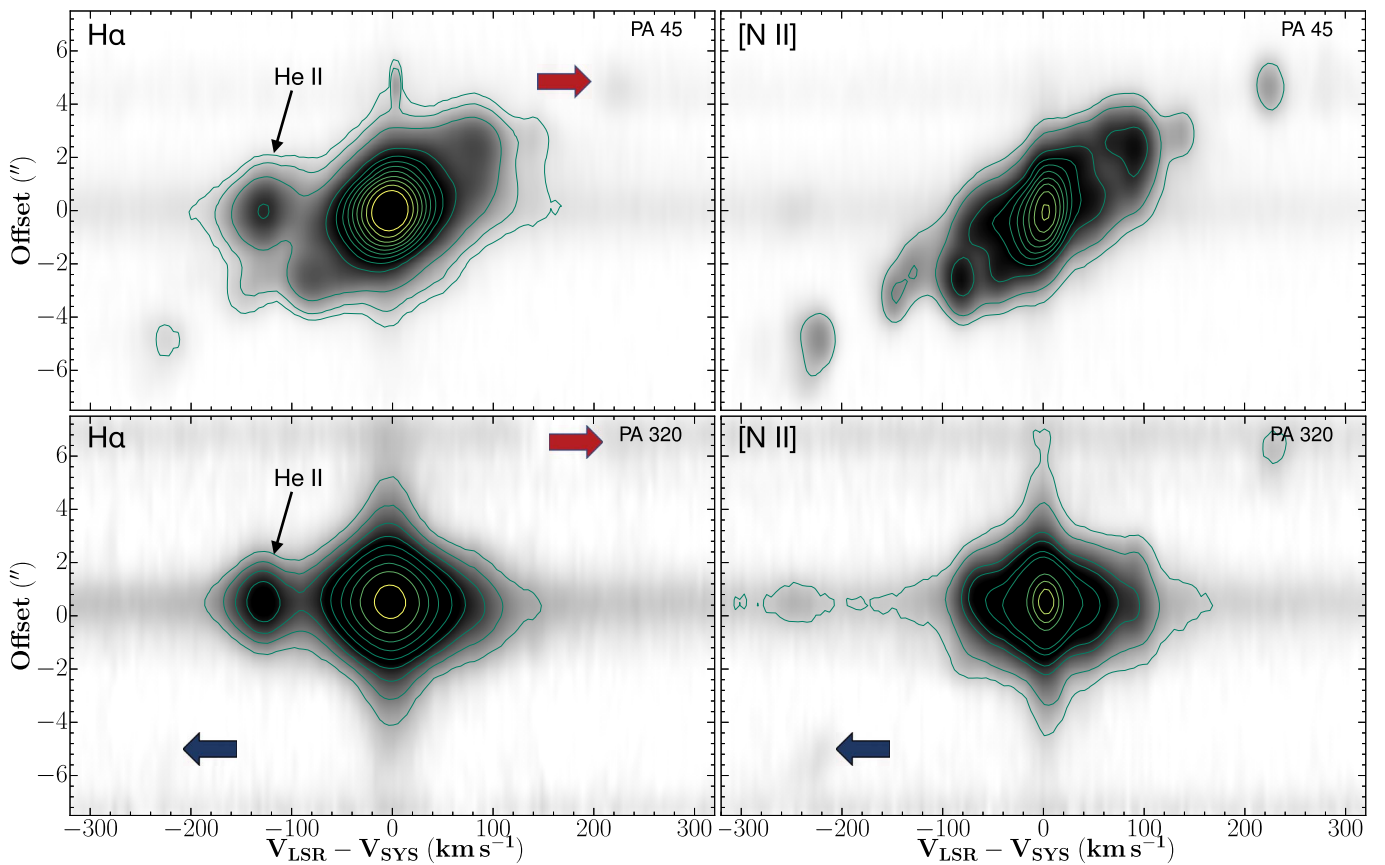


Figure 4. PV diagrams of the H α (left) and [N II] λ 6584 (right) emission lines extracted from MEGARA pseudo-slits along the bipolar axis at PA 45° (top) and an orthogonal direction at PA 320° (bottom). Colored contours are used to emphasize both faint and bright emission. When the emission from the high-velocity components (see text) is too faint to be shown by these contours, red and blue arrows are used to indicate receding and approaching features.

(Figure 5, top-left panel). In both amplitude spectra (Figure 5, right panel), we found the highest-amplitude frequency at 0.0565 cycles day $^{-1}$ to be significant, corresponding to a main period of \sim 17.7 days, and its first harmonic at 0.1199 cycles day $^{-1}$, corresponding to a \sim 9.0 day period. We note that the analysis of the same Kepler/K2 data by Jacoby et al. (2021) deemed it nonvariable, as these authors conservatively excluded cases of low-amplitude variability if the best period was close to or more than half of the sampling window, which could have resulted from spurious variability.

Figure 5, bottom-left panel, shows the folded individual and one-day binned light curve to the main frequency, as well as the mean values for 0.01-phase bins for better appreciation. The light curve shows a dominant peak at phase 0.2 with the main minimum at phase 0.0 and a subtle one at phase 0.55. Within the limits of the low signal, there seems to be a hint of a secondary peak at phase 0.75. The CSPN of M 3–38 is classified as an H-deficient, weak-emission-line star (DePew et al. 2011), but the coherence of its light curve precludes wind variability (see, for instance, the light curve of H 2–48 in Figure 3c of Jacoby et al. 2021), whereas long-lived bright spots on

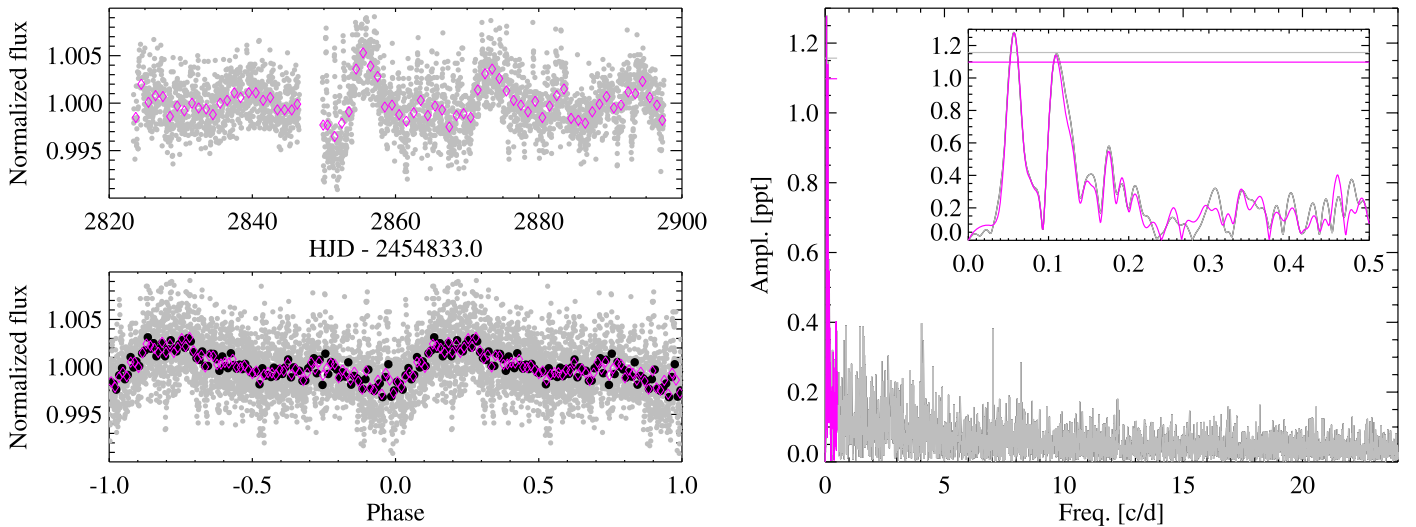


Figure 5. Top-left panel: original (gray) and one-day (magenta) binned Kepler/K2 C111 and C12 light curve of the CSPN of M 3–38. The two campaigns are separated by a three-day gap. Bottom-left panel: light curve of the CSPN of M3–38 folded into 17.7 days (symbols are the same as in the upper plot). Black points correspond to 0.01-phase binned data. Right panel: amplitude spectra for the individual and one-day binned data sets. The horizontal lines in the amplitude spectra are four times the mean amplitude in a 0.5 c/d range around the main frequency. The inset zooms in on the amplitude spectra up to the Nyquist frequency of the binned data series.

the stellar surface would have resulted in shorter periods associated with the stellar rotation. The variations in the light curve of M 3–38 could be attributed to irradiation onto a companion, as an ellipsoidal modulation due to tidal distortion would require a much shorter period.

4. Discussion

In the previous section, we have discussed the presence of a fast collimated outflow and a binary star in M 3–38. Their properties are discussed below.

The main outflow of M 3–38 is aligned along its bipolar axis and has expansion velocities up to $\approx 225 \text{ km s}^{-1}$ (Figures 2 and 4). This makes the outflow in M 3–38 one of the fastest among PNe, only surpassed by those in M1–16 and MyCn 18 and as fast as that in KjPn 8 (Guerrero et al. 2020, and references therein). The high-velocity, linear PV diagram, and the elongated morphology of this outflow make it a “bona fide” jet candidate. The jet space velocity cannot be derived because its inclination angle with the line of sight is unknown. If an inclination of $45^\circ \pm 15^\circ$ were to be adopted, then the space velocity of the jet would be $320_{-60}^{+130} \text{ km s}^{-1}$. The outermost fastest component of this jet is projected to be about $5''$ from the central star of M 3–38 (Figure 2). Adopting the most recent distance estimate of 8 kpc to M 3–38¹⁰ derived from MSX MIR flux densities by Ortiz et al. (2011) and a similar $45^\circ \pm 15^\circ$ inclination angle, the projected distance from the PN center of 0.19 pc would imply a true linear radius of $0.27_{-0.05}^{+0.11}$ pc. This translates into a jet kinematic age of 860_{-360}^{+630} yr. We remark that the values of the projected distance, true linear radius, and kinematic age given above scale with the distance, which has been adopted to be 8 kpc.

The ionized mass of the jet can be computed from the relationship (Pottasch 1984)

$$M_{\text{ion}} [M_{\odot}] = 11.06 \times F(\text{H}\beta) \frac{d^2 (T_e/10^4)^{0.88}}{N_e}, \quad (1)$$

where the intrinsic $\text{H}\beta$ flux is in units of $10^{-11} \text{ erg cm}^{-2} \text{ s}^{-1}$ and d in kiloparsec. The intrinsic $\text{H}\beta$ flux of the jet is derived to be $4.2 \times 10^{-12} \text{ erg cm}^{-2} \text{ s}^{-1}$ from the observed $\text{H}\alpha$ flux of $5.3 \times 10^{-13} \text{ erg cm}^{-2} \text{ s}^{-1}$ for a logarithmic extinction $c(\text{H}\beta)$ of 2.0 (Tylenda et al. 1992) and case B recombination. The density of the jet is $\approx 2,500 \text{ cm}^{-3}$, as derived from the density-sensitive $[\text{S II}]$ doublet (Figure 3, right). Assuming a value of 10,000 K for T_e , an ionized mass of $0.011 M_{\odot}$ is derived. Alternatively, the volume occupied by the jet and its density can be used to estimate the ionized mass assuming a conservative value of 0.1 for the “filling factor” ϵ and a standard value of 1.4 for the mean molecular weight. Adopting a single cylindrical geometry with a radius of $0''.5$ and height of $5''$ tilted by $45^\circ \pm 15^\circ$ with the line of sight, a value of $\approx 3 \times 10^{-3} M_{\odot}$ is derived. Given the uncertainties and assumptions of both methods, we shall adopt an intermediate value for the ionized mass of $M_{\text{ion}} = 6 \times 10^{-3} M_{\odot}$.

The values of space velocity,¹¹ kinematic age, and ionized mass can be combined to derive a mass-loss rate in the range of $2 \times 10^{-6} - 2 \times 10^{-5} M_{\odot} \text{ yr}^{-1}$, linear momentum from 6×10^{34} to $2.8 \times 10^{35} \text{ dyn}$, and mechanical luminosity of $2 - 20 L_{\odot}$ for the bulk of the emission.

The analysis of the Kepler/K2 light curve reveals a dominant frequency that corresponds to a period of 17.7 days, suggesting that M 3–38 host a binary system. The variability type is unclear as it can be assigned either to irradiation of a main-sequence companion (Hillwig et al. 2016b) or to ellipsoidal modulation, which is always interpreted in CSPNe

¹⁰ Distance estimates to M 3–38 in the literature range from 5.3 to 14.1 kpc, with an average value very similar to the one adopted in the text.

¹¹ An average radial expansion velocity of 70 km s^{-1} , which is representative of the bulk of emission, was adopted in the calculations of the linear momentum and mechanical luminosity, rather than the extreme 225 km s^{-1} expansion velocity.

as a case for a double degenerate system (DD; Hillwig et al. 2010). By adopting a total mass for the binary CSPN of M 3–38 of $0.7\text{--}1.6 M_{\odot}$ ($0.4\text{--}1.0 M_{\odot}$ for the CSPN and $0.3\text{--}0.6 M_{\odot}$ for the companion whether it is a WD or a main-sequence star), an orbital separation of $\approx 0.12\text{--}0.16$ au ($\approx 25\text{--}34 R_{\odot}$) is estimated. This orbital separation favors irradiation as a viable mechanism to produce the small amplitude variation seen in M 3–38 (see the top-left panel of Figure 1 in De Marco et al. 2008), whereas it makes ellipsoidal variability highly unlikely for the expected Roche lobe size of several solar radii.

The small orbital separation and the presence of highly collimated, fast ejecta from M 3–38 lead us to suggest that it might have formed as the result of CE evolution (e.g., Paczynski 1976; Ivanova et al. 2013; Jones & Boffin 2017). During the CE phase, the massive component overflows its Roche lobe and the companion is engulfed. Models predict that the orbit decays and orbital energy and angular momentum are transferred to the CE within a timescale of months to years (e.g., Chamandy et al. 2020). The subsequent evolution naturally explains the formation of bipolar ejecta (see, e.g., Zou et al. 2020; García-Segura et al. 2021; López-Cámara et al. 2022; Ondratschek et al. 2022 and references therein) of material in the direction perpendicular to the orbital plane (see Hillwig et al. 2016b). Indeed, high-resolution ALMA observations of water fountain objects, which are often interpreted as transitional sources between the AGB and proto-PNe phases, imply that they have experienced a recent (<200 yr) CE evolution (Khouri et al. 2021).

Mass estimates and kinematics of PNe that experienced a CE phase can be directly contrasted with theoretical predictions (Alcolea et al. 2007; Frew & Parker 2007; Corradi et al. 2015; Santander-García et al. 2022). The mass-loss rate of the jets of M 3–38 is about one to two orders of magnitude larger than those reported for the jets of PNe with post-CE close binaries (Tocknell et al. 2014) and for the jet in NGC 2392 (Guerrero et al. 2021), but consistent with those of the late AGB jets in BD+46°442 and IRAS 19135+3937 reported by Bollen et al. (2020). The linear momentum and mechanical luminosity of the jet in M 3–38 are at the high end of the range presented by those authors but still notably smaller than the values reported for outflows in proto-PNe (Bujarrabal et al. 2001).

If the jet in M 3–38 were launched by a CE interaction, its velocity should be of the order of the escape velocity of the secondary star launching the jet,

$$v_j = \sqrt{\frac{2GM}{R}}, \quad (2)$$

where M and R are its mass and radius, and G is the gravitational constant. Jet velocities of 540 and 480 km s^{-1} can be estimated for M5 V and M8 V stars with masses of 0.21 and $0.06 M_{\odot}$, respectively (see Cox 2000). These values are close to the upper limit estimated for the real jet velocity, but we note that the interaction of the jet with the material ejected previously during the AGB phase might have slowed it down.

The 17.7 days period proposed for the binary CSPN of M 3–38 is relatively long compared to the majority of binary CSPNe (see the compilation presented by Boffin & Jones 2019 and references therein). In contrast, simulations of CE evolution result in relatively large separations of the order of $10\text{--}20 R_{\odot}$ and periods larger than 3 days (see, e.g., Chamandy

et al. 2018; Iaconi & De Marco 2019; Chamandy et al. 2020), more like those of M 3–38.

To conclude, M 3–38 could be a new addition to the select group of PNe with fast collimated outflows and post-CE CSPNe (e.g., Fleming 1; Boffin et al. 2012). A more accurate characterization of the light curve of its CSPN and properties of its jet is urgent, as M 3–38 could be a case study of the late evolution of low- and intermediate-mass stars in binary systems and the launch of high-velocity jets in a CE phase. Its unusually long orbital period among binary post-CE CSPNe makes it also a key case for the comparison of CE evolution simulations and observations.

Finally, it is interesting to remark on the presence of an additional high-velocity ejecta that is almost orthogonal to the main one. While astonishing, this is not uncommon among PNe, with examples of collimated outflows almost orthogonal (e.g., IC 4593; Corradi et al. 1997) or along very different directions (see the compilation presented by Guerrero et al. (2021), with the record case of NGC 6210 with five different symmetry axes (Henney et al. 2021). It has been noted that jets misaligned with the main nebular axis might be characteristic of PNe with a post-CE binary (Bond & Livio 1990; De Marco 2009). There is no obvious interpretation for these phenomena (see, e.g., Bear & Soker 2017), but, if associated with a CE phase, it is clearly suggestive of dramatic changes in the preferential ejection direction of the stellar system.

J.S.R.G. acknowledges support from the Programa de Becas posdoctorales of the Direccion General de Asuntos del Personal Académico of the Universidad Nacional Autonoma de México (DGAPA, UNAM, Mexico). J.A.T. acknowledges support by the Marcos Moshinsky Foundation (Mexico), UNAM PAPIIT project IA101622 (Mexico), and the Visiting-Incoming program of the Centro de Excelencia Severo Ochoa (Spain). M.A.G. acknowledges support of grant PGC 2018-102184-B-I00 of the Ministerio de Educación, Innovación y Universidades cofunded with FEDER funds. C.R.-L. and M.A.G. acknowledge financial support from the State Agency for Research of the Spanish MCIU through the “Center of Excellence Severo Ochoa” award to the Instituto de Astrofísica de Andalucía (SEV-2017-0709). L.S. acknowledges support from UNAM PAPIIT grant IN110122. J.A.T. and G.R.-L. acknowledge support from CONACyT (grant 263373). The authors are thankful to the referee, Prof. Orsola De Marco, for comments and suggestions that improved the interpretation of the results presented here; to E. Rodríguez for helpful discussions on the binary nature of the CSPN of M 3–38; and to G. Jacoby and D. Jones for discussions and further clarification of the methods and results presented in their work (Jacoby et al. 2021). This work has made extensive use of the NASA’s Astrophysics Data System.

Facilities: Gran Telescopio Canarias (MEGARA), Kepler/K2, HST (WFPC2).


Software: megarars2cube.

ORCID iDs

J. S. Rechy-García  <https://orcid.org/0000-0002-0121-2537>

J. A. Toalá  <https://orcid.org/0000-0002-5406-0813>

M. A. Guerrero  <https://orcid.org/0000-0002-7759-106X>

C. Rodríguez-López  <https://orcid.org/0000-0001-5559-7850>

L. Sabin  <https://orcid.org/0000-0003-0242-0044>

G. Ramos-Larios  <https://orcid.org/0000-0003-2653-4417>

References

- Alcolea, J., Neri, R., & Bujarrabal, V. 2007, *A&A*, **468**, L41
- Balick, B. 1987, *AJ*, **94**, 671
- Bear, E., & Soker, N. 2017, *ApJL*, **837**, L10
- Boffin, H. M. J., & Jones, D. 2019, *The Importance of Binaries in the Formation and Evolution of Planetary Nebulae* (Cham: Springer)
- Boffin, H. M. J., Miszalski, B., Rauch, T., et al. 2012, *Sci*, **338**, 773
- Bollen, D., Kamath, D., De Marco, O., et al. 2020, *A&A*, **641**, A175
- Bond, H. E., & Livio, M. 1990, *ApJ*, **355**, 568
- Breger, M., Stich, J., Garrido, R., et al. 1993, *A&A*, **271**, 482
- Bujarrabal, V., Castro-Carrizo, A., Alcolea, J., et al. 2001, *A&A*, **377**, 868
- Chamandy, L., Blackman, E. G., Frank, A., et al. 2020, *MNRAS*, **495**, 4028
- Chamandy, L., Frank, A., Blackman, E. G., et al. 2018, *MNRAS*, **480**, 1898
- Corradi, R. L. M., García-Rojas, J., Jones, D., et al. 2015, *ApJ*, **803**, 99
- Corradi, R. L. M., Guerrero, M., Manchado, A., et al. 1997, *NewA*, **2**, 461
- Cox, A. N. 2000, in *Allen's Astrophysical Quantities*, ed. A. N. Cox, 1 (New York: Springer)
- De Marco, O. 2009, *PASP*, **121**, 316
- De Marco, O., Hillwig, T. C., & Smith, A. J. 2008, *AJ*, **136**, 323
- DePew, K., Parker, Q. A., Miszalski, B., et al. 2011, *MNRAS*, **414**, 2812
- Frew, D. J., & Parker, Q. A. 2007, in *Asymmetrical Planetary Nebulae, IV*, 475, <http://www.iac.es/proyect/apn4>
- García-Segura, G., Taam, R. E., & Ricker, P. M. 2021, *ApJ*, **914**, 111
- Giesekeing, F., Becker, I., & Solf, J. 1985, *ApJL*, **295**, L17
- Gil de Paz, A., Carrasco, E., Gallego, J., et al. 2018, *Proc. SPIE*, **10702**, 1070217
- Guerrero, M. A., Cazzoli, S., Rechy-García, J. S., et al. 2021, *ApJ*, **909**, 44
- Guerrero, M. A., Suzett Rechy-García, J., & Ortiz, R. 2020, *ApJ*, **890**, 50
- Guzman-Ramirez, L., Lagadec, E., Jones, D., et al. 2014, *MNRAS*, **441**, 364
- Henny, W. J., López, J. A., García-Díaz, M. T., et al. 2021, *MNRAS*, **502**, 1070
- Hillwig, T. C., Bond, H. E., Afşar, M., et al. 2010, *AJ*, **140**, 319
- Hillwig, T. C., Bond, H. E., Frew, D. J., et al. 2016a, *AJ*, **152**, 34
- Hillwig, T. C., Jones, D., De Marco, O., et al. 2016b, *ApJ*, **832**, 125
- Howell, S. B., Sobek, C., Haas, M., et al. 2014, *PASP*, **126**, 398
- Iaconi, R., & De Marco, O. 2019, *MNRAS*, **490**, 2550
- Ivanova, N., Justham, S., Chen, X., et al. 2013, *A&ARv*, **21**, 59
- Jacoby, G. H., Hillwig, T. C., Jones, D., et al. 2021, *MNRAS*, **506**, 5223
- Jones, D., & Boffin, H. M. J. 2017, *NatAs*, **1**, 0117
- Khoury, T., Vlemmings, W. H. T., Tafuya, D., et al. 2021, *NatAs*, **275**, 6
- Kuschnig, R., Weiss, W. W., Gruber, R., et al. 1997, *A&A*, **328**, 544
- Kwok, S. 2000, *The Origin and Evolution of Planetary Nebulae* (Cambridge: Cambridge Univ. Press)
- Lenz, P., & Breger, M. 2005, *CoAst*, **146**, 53
- López, J. A., Richer, M. G., García-Díaz, M. T., et al. 2012, *RMxAA*, **48**, 3
- López-Cámara, D., De Colle, F., Moreno Mendez, E., et al. 2022, *MNRAS*, **513**, 3634
- Luridiana, V., Morisset, C., & Shaw, R. A. 2015, *A&A*, **573**, A42
- Manchado, A., Guerrero, M. A., Stanghellini, L., et al. 1996, *The IAC morphological catalog of northern Galactic planetary nebulae* (Cambridge: Cambridge Univ. Press)
- Montoro-Molina, B., Guerrero, M. A., Pérez-Díaz, B., et al. 2022, *MNRAS*, **512**, 4003
- Ondratschek, P. A., Roepke, F. K., Schneider, F. R. N., et al. 2022, *A&A*, **660**, L8
- Ortiz, R., Copetti, M. V. F., & Lorenz-Martins, S. 2011, *MNRAS*, **418**, 2004
- Paczynski, B. 1976, in *IAU Symposium No. 73, Structure and Evolution of Close Binary Systems* (Dordrecht: Reidel), 75
- Pascual, S., Cardiel, N., Gil de Paz, A., et al. 2019, in *Highlights on Spanish Astrophysics X, Proc. of the Scientific Meeting of the Spanish Astronomical Society, XIII*, ed. B. Montesinos et al. (Almería: Spanish Astronomical Society), 227
- Pottasch, S. R. 1984, *Astrophysics and Space Science Library* (Dordrecht: Reidel)
- Rechy-García, J. S., Guerrero, M. A., Duarte Puertas, S., et al. 2020a, *MNRAS*, **492**, 1957
- Rechy-García, J. S., Guerrero, M. A., Santamaría, E., et al. 2020b, *ApJL*, **903**, L4
- Rechy-García, J. S., Toalá, J. A., Cazzoli, S., et al. 2021, *MNRAS*, **508**, 2254
- Rechy-García, J. S., Velázquez, P. F., Peña, M., et al. 2017, *MNRAS*, **464**, 2318
- Sahai, R., & Trauger, J. T. 1998, *AJ*, **116**, 1357
- Santander-García, M., Jones, D., Alcolea, J., et al. 2022, *A&A*, **658**, A17
- Schwarz, H. E., Corradi, R. L. M., & Melnick, J. 1992, *A&AS*, **96**, 23
- Soker, N. 1997, *ApJS*, **112**, 487
- Tocknell, J., De Marco, O., & Wardle, M. 2014, *MNRAS*, **439**, 2014
- Tylenda, R., Acker, A., Stenholm, B., et al. 1992, *A&AS*, **95**, 337
- Vassiliadis, E., & Wood, P. R. 1993, *ApJ*, **413**, 641
- Zou, Y., Frank, A., Chen, Z., et al. 2020, *MNRAS*, **497**, 2855